Droplet motion in a microconfined shear flow via a three-dimensional spectral boundary element method

Mohammad A. Khan and Yechun Wang[a)]
Department of Mechanical Engineering, North Dakota State University, Dept. 2490, P.O. Box 6050, Fargo, North Dakota 58108, USA

(Received 23 May 2010; accepted 17 November 2010; published online 9 December 2010)

A 3D spectral boundary element method is employed to compute the dynamics of a single droplet in a microconfined shear flow. Comparisons have been made for the motion of an initially spherical droplet near a single wall and that between two parallel plates. Investigations are conducted for the influences of the capillary number, viscosity ratio, and initial location of the droplet on the droplet deformation, orientation, velocities, as well as the transition between the initial rapid deformation and the subsequent relaxation stage. Computational results for the deformation and velocities are compared with analytical predictions. It is found that the analytical predictions are limited for small deformations, large droplet-wall distances, and near equiviscous droplets. © *2010 American Institute of Physics*. [doi:10.1063/1.3525357]

I. INTRODUCTION

The fundamental study on the motion of a neutrally buoyant droplet in a low-Reynolds-number shear flow near solid walls can be traced back to 1980s with applications in lubrication technologies,[1,2] where the existence of journal bearing walls significantly influences droplet-containing lubricants. More recently, technologies utilizing nanoliter sized droplets have been developed (e.g., microfluidics) which significant applications in biochemical processes, biomedical research, and clinical studies, including enzymatic analysis, DNA analysis, and disease diagnosis.[3–10] To provide fundamental understanding of the motion of droplets in the aforementioned systems, thorough investigations on the nature of droplet motion near the vicinity of a microfluidic wall are thus demanded. Investigations have been focused on the motion of a droplet between two parallel plates employing the following dimensionless parameters: (i) capillary number $\mathrm{Ca}=\mu Ga/\gamma$ where μ is the viscosity of the suspending fluid, a the radius of the undeformed droplet, G the shear rate, and γ the surface tension at the droplet interface; (ii) the viscosity ratio λ between the droplet and the suspending fluid; (iii) the distance between the droplet and one of the plates normalized by the droplet size; (iv) the gap between plates (normalized by the droplet size). Numerical work and experimental studies have been devoted to droplet moving along the center line of the gap between the parallel plates.[11–16] Larger deformation is observed for droplet in shear flow confined by parallel plates than unconfined flows.[11,12] An increase in droplet deformation is observed for decreasing gap width. The droplet is found to orient toward the flow direction.[13] For moderate capillary numbers, droplets with a viscosity ratio $\lambda \leq 1$ display an "overshoot" in the deformation at early stage of the process for small gaps. For droplet with $\lambda > 1$, overshoots in droplet deformation takes place for large gaps.[14] Critical capillary numbers (Ca_c), above which the droplet will break up, are found as a function of the gap width. For capillary numbers smaller than the critical value, the equilibrium droplet deformation shows a linear relation with the capillary number.[15] The critical capillary numbers are experimentally found to be influenced by gap width as well as the viscosity ratio λ.[12,16]

Few studies have investigated the motion of a droplet moving near a single solid wall in shear flow or the case when the droplet is released at a location which deviates from the centerline of the gap, although these cases can help us understand the migration of droplet perpendicular to the solid wall. Theoretical work by Leighton and Acrivos[17] examined the lift on a nondeformable spherical particle in a shear flow confined by a single plate. Scaled with the longitudinal drag, the lift was found to be linear with the Reynolds number. The authors concluded that the lift as a result of the inertia in a low-Reynolds-number flow can be ignored due to the small magnitude. However their focus was on spherical particles hence the lateral migration due to particle deformation was not investigated. Based on Taylor's small deformation theory, Shapira and Haber[2] derived the droplet deformation and drag force as a function of capillary number, viscosity ratio and droplet-to-wall distance for a droplet moving near a single wall or between parallel plates. Smart and Leighton, Jr.[18] experimentally investigated the motion and deformation of a droplet with viscosity ratio $\lambda=0.08$ in a Couette flow. Uijttewaal *et al.*[19,20] investigated the droplet lateral and longitudinal migration near a single solid wall in shear flow using a boundary integral method with triangular discretization. They compared the numerical solution for the migration velocities with analytical predictions. However, the droplet deformation presented in their study was based on a quasistatic assumption. Somewhat related are studies for the droplet motion in a Poiseuille flow between parallel plates. The results for droplet motion in close vicinity to one of the plate could be valuable since the flow close to the plate could be considered linear. For example, Griggs *et al.*[21] numerically investigated the motion of droplet subject to a

[a)]Electronic mail: yechun.wang@ndsu.edu.

 © 2010 American Institute of Physics

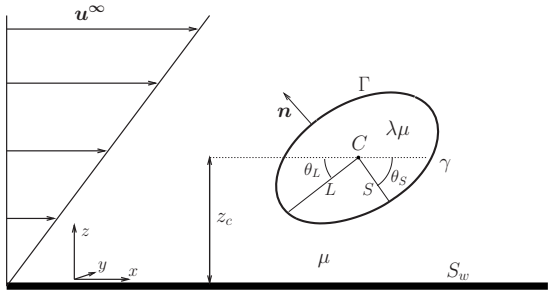

FIG. 1. Illustration for a droplet moving near a solid wall in shear flow.

low-Reynolds number Poiseuille flow between parallel plates under the influence of the capillary number, viscosity ratio, gap width, as well as the initial location of the droplet in the gap. They found that for droplet placed off the centerline, regardless of the initial location, capillary number, or viscosity ratio, deformable droplets tend to migrate away from the plate nearer to the droplet. Nonmonotonic relation is observed between the migration velocity of the droplet away from the wall and the viscosity ratio for $2 \leq \lambda \leq 10$.

In this study, a 3D spectral boundary element method is, for its first time, employed to investigate the behavior of a deformable droplet driven to move via a low-Reynolds-number shear flow near a single solid wall. The purposes of the current study is to (i) validate the successful application of the recently developed 3D spectral boundary element method, a high-order boundary integral method, on droplet motion in a wall-bounded shear flow, (ii) provide numerical evidence on the justification for neglecting the solid boundary far from the droplet in numerical studies, since in experiments two plates are needed to create the shear flow, e.g., using a Couette device, and (iii) investigate the influence of capillary number, viscosity ratio, and initial location of the droplet on the droplet deformation and migration velocities. We emphasize that different from previous numerical studies we employ a spectral method which leads to higher accuracy and exponential convergence.

II. MATHEMATICAL FORMULATION

We consider that a neutrally buoyant droplet with viscosity $\lambda\mu$ is suspended in another immiscible fluid with viscosity μ, as shown in Fig. 1. Far from the droplet a shear flow with shear rate G is applied. The surface tension γ of the droplet interface is assumed constant. The initially spherical droplet is released with its centroid at a distance z_{c0} to the solid wall S_w. In this work, we use the radius of an undeformed spherical droplet a as the length scale and the viscous time scale $1/G$ as the time scale. The velocity is scaled with aG. The parameters that influence the droplet behavior are the capillary number $\mathrm{Ca}=\mu Ga/\gamma$, viscosity ratio λ, and the initial distance between the solid wall and the droplet centroid z_{c0}. The droplet deformation is quantified by defining

$$D = \frac{L-S}{L+S}, \tag{1}$$

where L is the length of the longest axis of the droplet and S is the shortest as shown in Fig. 1. Both L and S are measured from the center of the mass of the droplet. The droplet orientation could be described using the orientation angles θ_L and θ_S, which are defined by the angle between the long axis and the negative x axis and the angle between the short axis and the positive x axis, respectively. Due to the shear flow and the deformation of the droplet itself, the droplet migrates with a velocity which is composed by a velocity along the solid wall (U_x) and a velocity perpendicular to the wall (U_z).

For a micron sized droplet, the inertia may be ignored due to the low-Reynolds number. Due to the low-Reynolds number (i.e., small size and velocity), viscous fluids (e.g., PDMS or silicone oil) are typically used to create a moderate value for the capillary number. The governing equations are thus the Stokes equation and the continuity,

$$\nabla \cdot \boldsymbol{\sigma} = -\nabla p + c\nabla^2 \boldsymbol{u} = \boldsymbol{0}, \tag{2}$$

$$\nabla \cdot \boldsymbol{u} = 0, \tag{3}$$

where $c=1$ for the suspending fluid and $c=\lambda$ for the fluid in the droplet.

The boundary conditions on the droplet interface are

$$\boldsymbol{u} = \boldsymbol{u}_1 = \boldsymbol{u}_2, \tag{4}$$

$$\Delta \boldsymbol{f} \equiv \boldsymbol{f}_2 - \boldsymbol{f}_1 = \frac{1}{\mathrm{Ca}}(\nabla_S \cdot \boldsymbol{n})\boldsymbol{n}, \tag{5}$$

where the subscripts "1" and "2" represent the flow inside the droplet and the suspending fluid, respectively. The unit normal is defined to point into the suspending fluid and is designated as $\boldsymbol{n}$. The curvature is thus expressed as $\nabla_S \cdot \boldsymbol{n}$. For the boundary over the solid plate, the no-slip condition applies, $\boldsymbol{u}=\boldsymbol{0}$. The undisturbed velocity ($\boldsymbol{u}^\infty$) and stress ($\boldsymbol{f}^\infty$) of shear flow are applied as

$$\boldsymbol{u}^\infty = (z,0,0), \tag{6}$$

$$\boldsymbol{f}^\infty = \boldsymbol{\sigma}^\infty \cdot \boldsymbol{n}. \tag{7}$$

The governing equations and boundary conditions could be transformed into boundary integral equations (BIE).[22] We derive that the velocity at an arbitrary point $\boldsymbol{x}_0$ on the droplet interface Γ or on the solid wall S^w satisfies the following boundary integral equation:

$$\begin{aligned}\Omega \boldsymbol{u}(\boldsymbol{x}_0) - \Omega_0 \boldsymbol{u}^\infty(\boldsymbol{x}_0) &= -\int_\Gamma \{\boldsymbol{S}\cdot(\Delta \boldsymbol{f} - \boldsymbol{f}^\infty) - \boldsymbol{T}\cdot[\boldsymbol{u}(1-\lambda) - \boldsymbol{u}^\infty]\cdot \boldsymbol{n}\} dS \\ &\quad - \int_{S_w} [\boldsymbol{S}\cdot(\boldsymbol{f}_2 - \boldsymbol{f}^\infty) - \boldsymbol{T}\cdot(\boldsymbol{u}_2 - \boldsymbol{u}^\infty)\cdot \boldsymbol{n}] dS,\end{aligned} \tag{8}$$

where $\Omega = 4\pi(1+\lambda)$ and 4π for $\boldsymbol{x}_0$ on Γ and the solid boundary, respectively; $\Omega_0 = 4\pi$ for all boundaries. Kernel $\boldsymbol{S}$ is the fundamental solution for the Stokes equations and $\boldsymbol{T}$ is the associated stress.

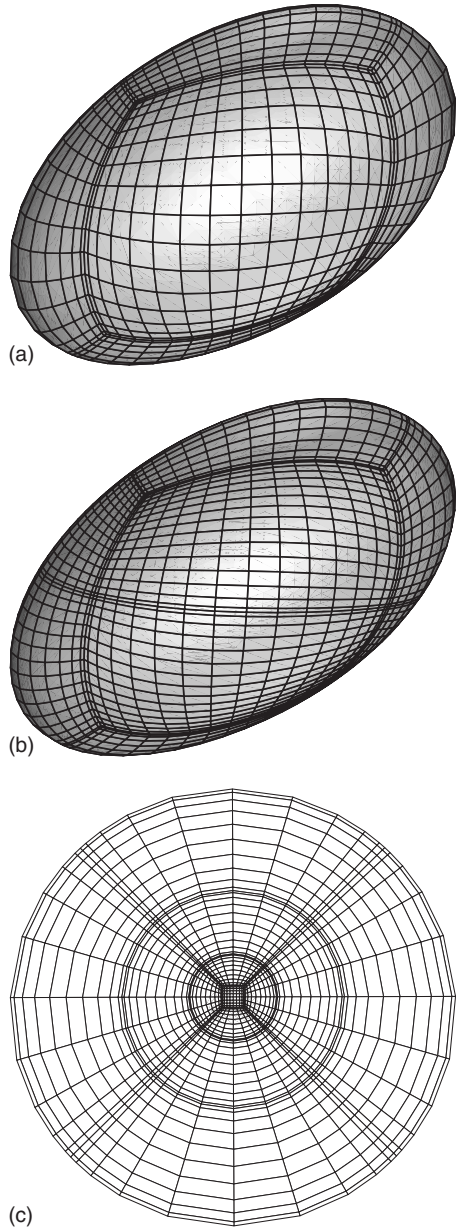

FIG. 2. Discretization of geometry for spectral boundary element calculation for a droplet moving near a solid plate in shear flow: (a) six spectral elements are employed on the droplet interface for the case of Ca=0.2, $\lambda=1$, and $z_{c0}=1.5$ at time $t=8$, (b) ten spectral elements on the droplet interface for Ca=0.3, $\lambda=1$, and $z_{c0}=1.5$ at time $t=1$, and (c) surface of the solid wall.

III. NUMERICAL METHOD

Details for the spectral discretization, mesh redistribution, and interfacial smooth schemes can be found in Wang and Dimitrakopoulos.[23] Nevertheless for the completeness of this study, in this section we summarize our numerical approach, address criteria for parameter selections, and present the convergence test results for the current problem.

The droplet interface is discretized into either six or ten quadrilateral spectral elements as shown in Figs. 2(a) and 2(b) using cube projection. The surface of the solid wall is composed of a central square element surrounded by three rows of four sectoral elements as shown in Fig. 2(c). The length of the center square element and the outer radius of each row of sectors are a, $2a$, $5a$, and $10a$, respectively (where a is the radius of an undeformed droplet). The center of the solid surface is always in alignment with the droplet centroid. Computations have been made for the wall radius $5 \leq R/a \leq 20$, where R denotes the radius of the solid wall and droplet-wall distance $1.02 \leq z_{c0}/a \leq 10$. The relative errors of droplet deformation and velocities are calculated using values for $R=20a$ as the base. We found that the relative errors for all deformation and velocities when $R \geq 10a$ are less than $O(10^{-4})$. Hence, although the solid wall should extend to infinity, we define in this numerical study a wall radius ten times the undeformed droplet radius for the solid wall.

The geometric variables on each element are discretized via Lagrange interpolations using two parametric variables on a square interval $[-1,1]^2$. The basis points for the parametric variables are zeros of N_B-order orthogonal polynomials (i.e., spectral points). The geometric and physical information on each discretized node is then substituted into the boundary integral equations. By rearrangement and collection of terms, a linear system of algebraic equations relating the velocity $\boldsymbol{u}$ and normal stress $\boldsymbol{f}$ is formed $\boldsymbol{u}=\boldsymbol{A}\boldsymbol{f}+\boldsymbol{B}\boldsymbol{u}$. The matrices $\boldsymbol{A}$ and $\boldsymbol{B}$ are given by the integration of the kernels $\boldsymbol{S}$ and $\boldsymbol{T}$ and the basis function. The integrations are obtained via Gauss quadrature using Legendre and Lobatto points. A fourth-order Runge–Kutta algorithm with a time step of 5×10^{-4} is used for the time evolution of the interface geometry ($\boldsymbol{x}$) via the kinematic condition given by

$$\frac{d\boldsymbol{x}}{dt} = (\boldsymbol{u}\cdot\boldsymbol{n})\boldsymbol{n} + U_t\boldsymbol{t}, \tag{9}$$

$$U_t = c_t(\boldsymbol{u}\cdot\boldsymbol{t}) + (1-c_t)(\boldsymbol{u}_c\cdot\boldsymbol{t}), \tag{10}$$

where $\boldsymbol{t}$ is a unit tangent vector on the interface and $\boldsymbol{u}_c$ is the velocity of the droplet centroid. The interface evolution is determined by the first term on the right hand side of Eq. (9), while the second term utilizes the velocity tangent to the interface for mesh redistribution. Parameter c_t $(0 \leq c_t \leq 1)$ is employed to avoid severe grid distortion due to the movement of droplet centroid. In addition, a first-order smoothing scheme is applied for better stability of the numerical method. Details for the choice of spectral points, the numerical implementation of mesh redistribution, and the interfacial smoothing scheme can be found in Wang and Dimitrakopoulos.[23]

Convergence tests have been performed to assess the accuracy of the computational results. The droplet deformation D as well as the lateral velocity U_z have been computed using $N_B=7$, 9, 11, 13, and 15 spectral points for each element. Other parameters are Ca=0.2, $\lambda=1$, and $z_{c0}=1.5$. The droplet interface is composed of $N_E=6$ spectral elements. The relative error in D and U_z is determined using those at $N_B=15$ as the base and is plotted as a function of $N=N_E N_B^2$ in Fig. 3. An exponential convergence has been observed for both the deformation and the droplet velocity. For the computations in this study, $N_B=11$ has been employed which gives an accuracy in the order of magnitude of 10^{-4}.

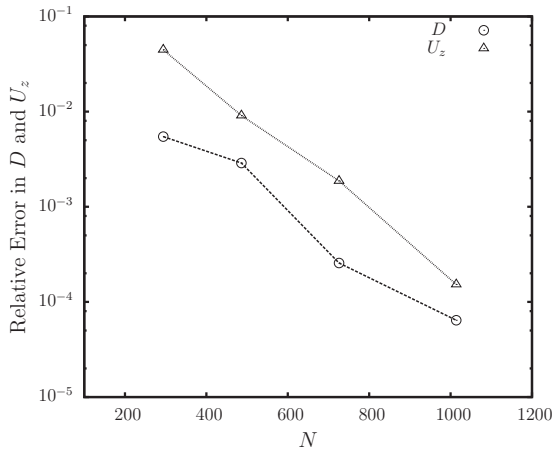

FIG. 3. The relative error in the computed deformation D and droplet velocity in the z direction vs the number of spectral points employed on the droplet $N=N_E N_B^2$ for Ca=0.2, $\lambda=1$, and $z_{c0}=1.5$ at time $t=4$. The convergence shown is generated by using $N_E=6$ elements on the droplet and $N_B=7$, 9, 11, and 13. The results for $N_B=15$ are used to determine the numerical error.

IV. RESULTS AND DISCUSSION

Employing the 3D spectral boundary element method described in the previous section, we compute the motion of an initially spherical droplet in a shear flow after it is released at a distance z_{c0} to a single solid wall. The droplet moves along the solid wall due to the exerted shear flow while it migrates away from the wall. In this section, we first compare the droplet deformation and motion in a vicinity of a single solid wall with similar situations for a droplet moving closer to one of two parallel plates. Validation has been made by comparing our results to both numerical and experimental findings in literature. We then investigate and discuss the influence of the capillary number, viscosity ratio, and initial droplet location on the droplet deformation, orientation, longitudinal velocity, and lateral velocity. In addition, the two stages of droplet behavior, the initial rapid deformation and the subsequent relaxation, have been distinguished and discussed.

A. Droplet motion between parallel plates

In this work, we focus on the behavior of the droplet in a close vicinity of a stationary solid wall. The effect of any faraway wall or plate is ignored. The validity of this assumption is concluded via the comparison with computations for droplet motion in two parallel plates. The boundary integral equation for the case of parallel plates is identical to Eq. (8). The boundary conditions on the droplet interface also follow Eqs. (4) and (5). No-slip conditions are applied for both the top plate, $\boldsymbol{u}=(z_{\text{plate}},0,0)$, and the lower plate, $\boldsymbol{u}=(0,0,0)$. The discretization for the top plate is similar to the lower plate as indicated in Fig. 2(c).

As shown in Fig. 4, we plot the droplet deformation D, lateral migration velocity U_z, and longitudinal velocity U_x as functions of time for droplet moving in two parallel plates with L_t as the distance between the top plate and the original location of the droplet. The separation between the lower plate and the droplet initial location is always $z_{c0}=1.5$ in this section. In Fig. 4, we also include our computation for a droplet moving near a single wall with an initial distance $z_{c0}=1.5$. For all cases, the capillary number is Ca=0.1 and the viscosity ratio is $\lambda=1$. We vary the distance L_t and found that droplet deformation monotonically decreases as we increase L_t for $L_t<10$. For $L_t\geq 10$, the deformation is independent on L_t and the computational result agrees with that for a single solid wall. The lateral velocity U_z approaches zero and maintains negligibly small for a droplet released at the center of two parallel plates (i.e., $L_t=1.5$). As we increase L_t, U_z

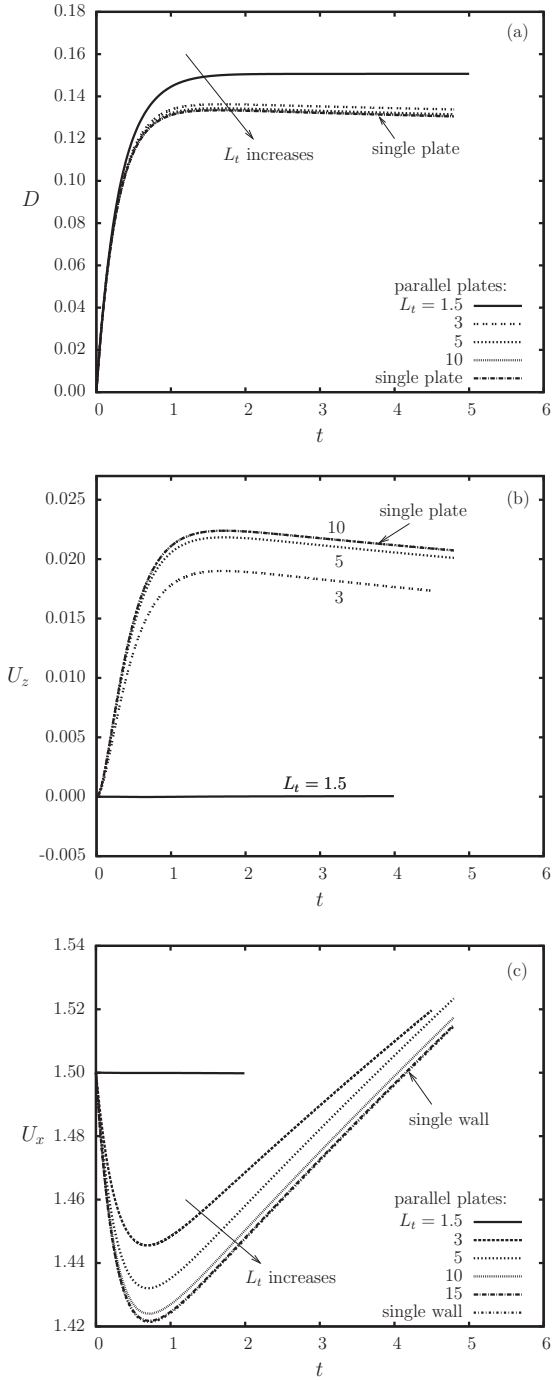

FIG. 4. Transient behaviors of deformation D, lateral velocity U_z, and longitudinal velocity U_x of a droplet moving near a single solid wall and between two parallel plates. The distance between the top plate and the initial location of the droplet is denoted as L_t.

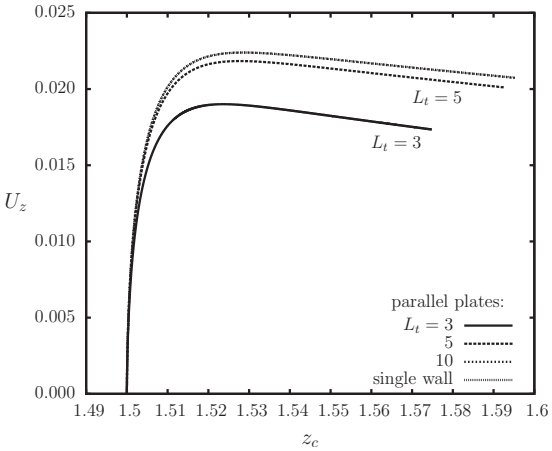

FIG. 5. Lateral velocity U_z as a function of droplet-wall distance z_c for a droplet moving near a single solid wall and between two parallel plates. The distance between the top plate and the initial location of the droplet is denoted as L_t.

monotonically increases for $L_t < 10$. For $L_t \geq 10$, the computational result for U_z is close to that of a single wall. We also plot U_z as a function of the droplet-wall distance z_c in Fig. 5. The lateral velocity U_z first increases abruptly and then slowly decreases as the droplet moves toward the upper wall. For the case when $L_t = 1.5$, U_z is independent on z_c and the value is negligibly small. If the initial location of the droplet is at the centerline between the two parallel plates, the longitudinal velocity U_x of the droplet centroid is found to be the undisturbed flow velocity of the suspending fluid at the same location and is independent on the time. The velocity U_x decreases with the increase of L_t for $L_t < 15$. For $L_t \geq 15$, U_x is computed to be identical with that of a single wall.

For validation we compare our solution to both the computational and experimental results by Vananroye *et al.*[13] for a droplet moving in the centerline of the gap created by parallel plates. Figure 6 shows the comparison for Ca=0.2, $\lambda = 1$, and $z_{c0} = L_t = 1.136\,36$. Data are measured from Fig. 10(a) of Vananroye *et al.*[13] and converted using the time scale and length scale defined in the current study. Good

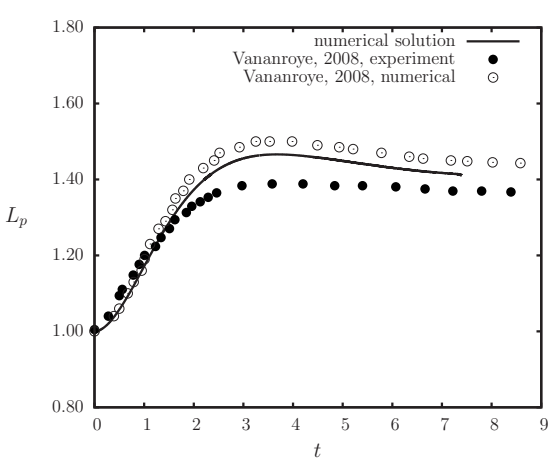

FIG. 6. Droplet length L_p as a function of time t for Ca=0.2, $\lambda = 1$, and $z_{c0} = L_t = 1.136\,36$. Also included are the experimental measurements and numerical results by Vananroye *et al.* (Ref. 13).

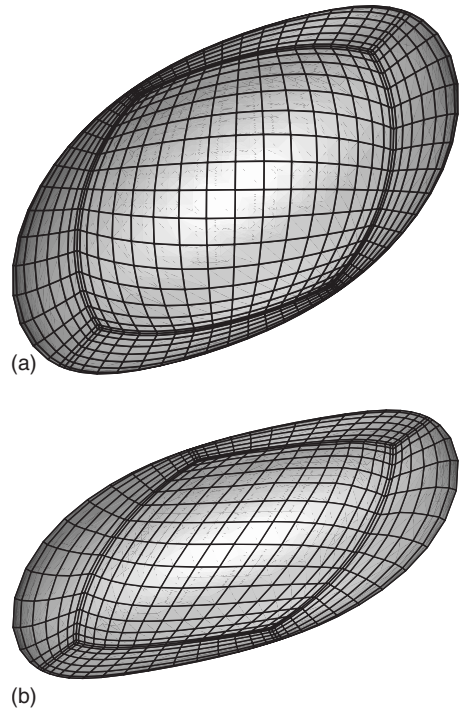

FIG. 7. Numerically computed droplet geometries at time $t = 1.02$ and 4.24 for Ca=0.2, $\lambda = 1$, and $z_{c0} = L_t = 1.136\,36$. Good agreement has been found by comparing to Figs. 10(b1) and 10(b2) of Vananroye *et al.* (Ref. 13).

agreement has been found for the droplet length L_p on the vorticity-velocity plane as defined in Vananroye, Puyvelde, and Moldenaers.[16] As shown in Fig. 7 the droplet shapes at time $t = 1.02$ and 4.24 computed in the current study also demonstrate good agreement with the experimental images taken by Vananroye *et al.*[13] [Fig. 10(b) in their study].

B. Influence of the capillary number

As the droplet is translating near a solid wall, the droplet undergoes deformation and rotation. We describe the droplet geometry via droplet deformation D and rotation angles θ_L and θ_S. As shown in Fig. 8, lengths of droplet axes (L and S), deformation (D), and orientation angles (θ_L and θ_S) have been plotted as functions of time after the onset of the shear flow at $t = 0$. The droplet deformation increases drastically at the beginning and then experiences a slow relaxation after the maximum deformation is reached. The sudden increase in the deformation is resulted from the increase of the length axis and the decrease of the short axis. The increment in the long axis is more prominent than the short axis. In the relaxation process, the long axis L decreases and the short axis S increases slowly. Correspondingly, as it fast deforms the droplet rapidly rotates toward the flow direction and then the droplet rotates slowly during the relaxation. The orientation angle for the short axis, θ_S, increases to its maximum and then slowly decreases back, however, the angle for the long axis, θ_L, continues to decrease slowly after the initial rapid decreasing. A variety of capillary numbers is employed in the computation. Results for three capillary numbers Ca=0.05, 0.1, and 0.2 are presented in Fig. 8. The droplet experiences larger deformation at larger values for Ca. We plot in Fig. 9

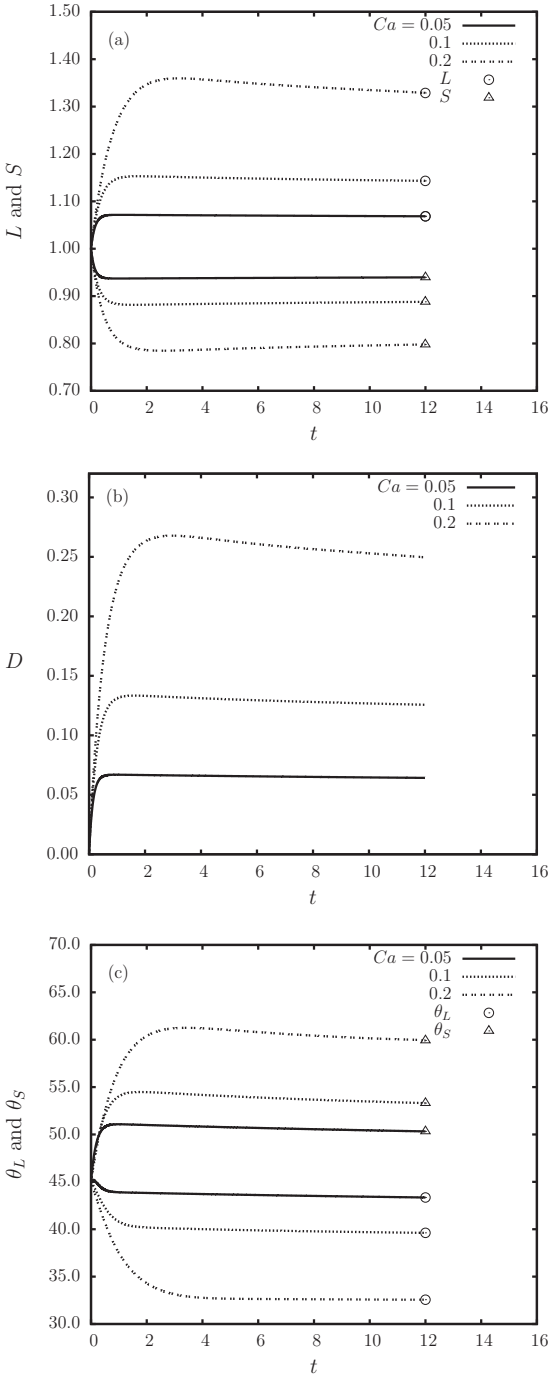

FIG. 8. The time evolution of (a) long L and short S axes of droplet, (b) the deformation D, and (c) the orientation of the long and short axes θ_L and θ_S. Three capillary numbers are included for comparison: Ca=0.05, 0.1, and 0.2. For all cases, $\lambda=1$ and $z_{c0}=1.5$.

the deviation of the deformation D from that of a fully relaxed droplet D_{zc} at the same location for the droplet centroid as a function of time. The abrupt decrease in the deformation difference indicates the beginning of the relaxation process. (D_{zc} is obtained by computing the deformation of a droplet released at $z_{c0}=1.3$.) Figure 8(b) and more clearly Fig. 9 show that the maximum deformation is reached earlier and the relaxation process starts earlier for smaller capillary numbers.

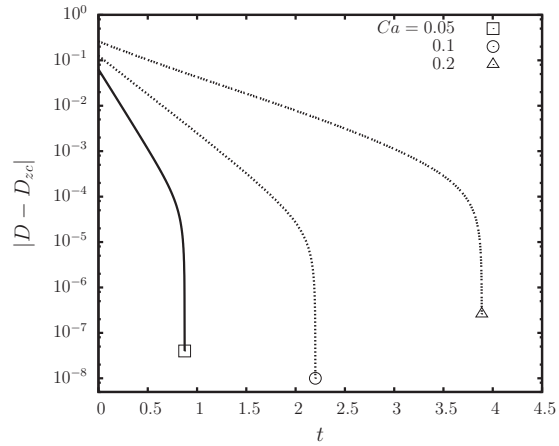

FIG. 9. Deviation of the droplet deformation from the relaxation deformation $|D-D_{zc}|$ as a function of time. Three capillary numbers are included for comparison: Ca=0.05, 0.1, and 0.2. For all cases, $\lambda=1$ and $z_{c0}=1.7$.

The lateral migration velocity of the droplet U_z is observed to behave similarly to the deformation D. As shown in Fig. 10(a), the lateral velocity increases rapidly to reach its maximum immediately after the onset of the shear flow, and then the velocity decreases during the relaxation. As shown in Fig. 11(a), the lateral velocity U_z increases with the in-

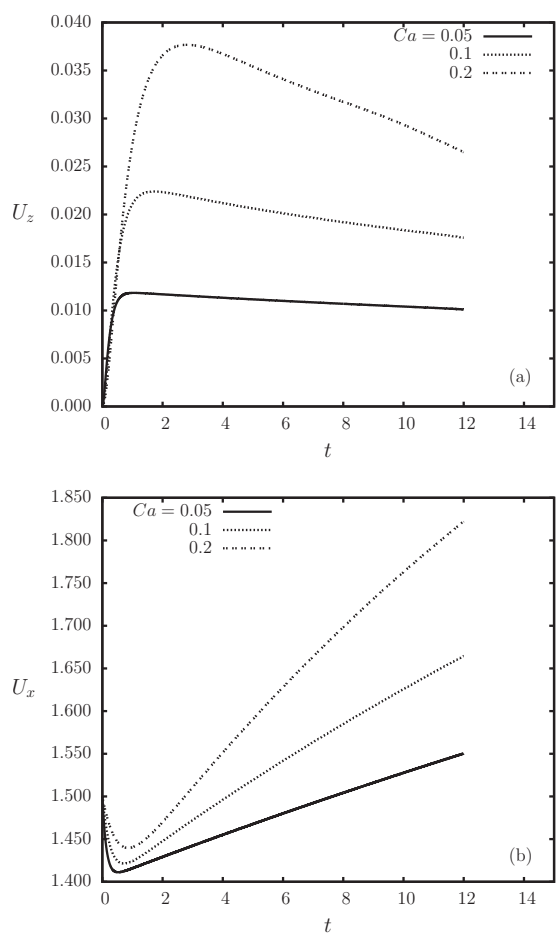

FIG. 10. Droplet centroid velocity as a function of time t: (a) the lateral velocity U_z and (b) the longitudinal velocity U_x. Ca=0.05, 0.1, and 0.2. For all cases, $\lambda=1$ and $z_{c0}=1.5$.

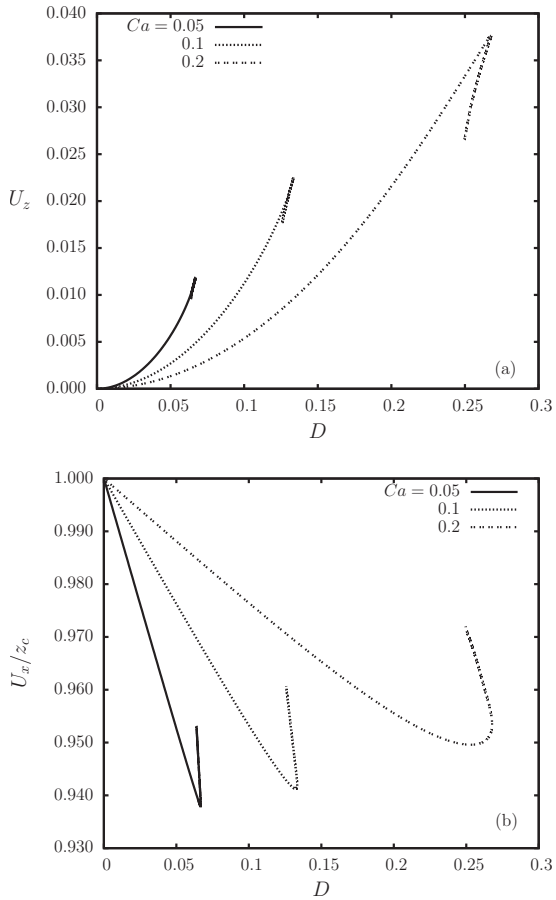

FIG. 11. Droplet centroid velocity as a function of deformation D: (a) the lateral velocity U_z and (b) the longitudinal velocity U_x. Ca=0.05, 0.1, and 0.2. For all cases, $\lambda=1$ and $z_{c0}=1.5$.

crease of the deformation before the maximum U_z (i.e., the maximum D) is reached, and then U_z decreases with the decrease of the deformation during relaxation. Considering different values for the capillary number, we observe that the smaller deformation induced by smaller capillary number leads to slower migration in the lateral direction, i.e., small U_z. No lateral migration is observed for nondeformable spherical droplets due to the reversibility of the Stokes equations. Hence, the lateral migration of the droplet is determined or induced by the deformation of the droplet.

As shown in Fig. 10(b), the longitudinal velocity of the droplet centroid U_x starts with the same value with the flow velocity of the suspending fluid and decreases slightly after the onset of the flow, but then increases significantly after a minimum value is reached. We also plot the velocity U_x, normalized by the undisturbed flow velocity of the suspending fluid at the droplet centroid z_c, as a function of the deformation D in Fig. 11(b), we observe that as flow distorts the droplet (i.e., D increases), the velocity U_x decreases and the droplet lags behind the bulk flow. When the droplet starts to relax (i.e., D decreases gradually), U_x increases significantly. The influence of the droplet deformation on the longitudinal velocity U_x is more prominent for smaller capillary numbers.

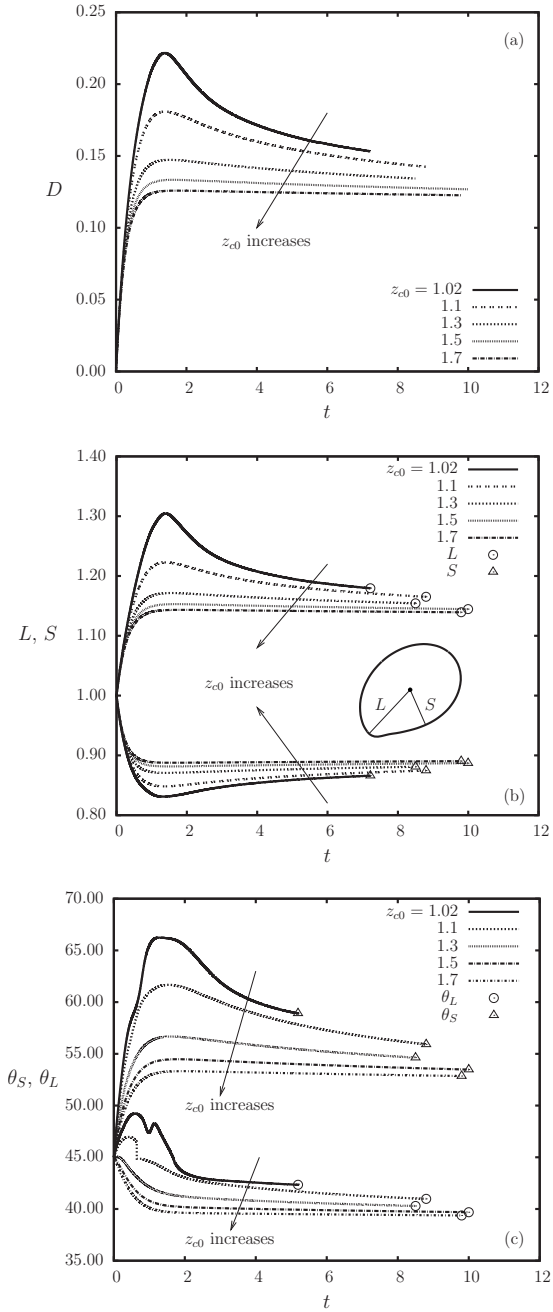

FIG. 12. The time evolution of (a) the deformation D, (b) long L and short S axes of the droplet, and (c) the orientation angles of the axes θ_L and θ_S. Various initial droplet-wall distances are included $z_{c0}=1.02$, 1.1, 1.3, 1.5, and 1.7 for Ca=0.1 and $\lambda=1$. The inset in (b) shows the droplet profile at its largest deformation for $z_{c0}=1.02$ as well as the long axis L and the short axis S at this moment.

C. Influence of initial location of the droplet

The influence on the droplet-wall distance on the droplet deformation is investigated as shown in Fig. 12(a). The droplet experiences an overshoot in deformation upon release due to the strong hydrodynamics interaction with the solid wall. And the overshoot is much more prominent for a droplet released at a closer distance to the wall. A slower retraction takes place after the maximum deformation is achieved as the droplet moves away from the wall. The retraction process appears to act faster for a smaller initial droplet-wall dis-

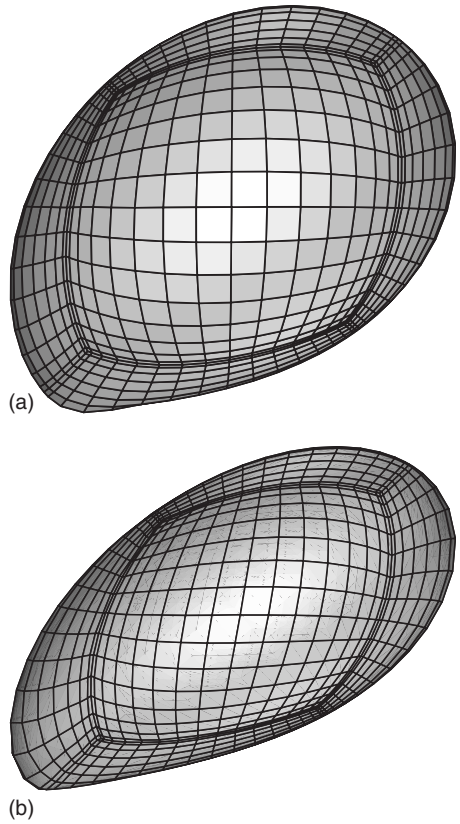

FIG. 13. Shapes of droplet at its largest deformation. (a) Ca=0.1, λ=1, z_{c0}=1.02, and t=1.4; (b) Ca=0.2, λ=1, z_{c0}=1.02, and t=1.8.

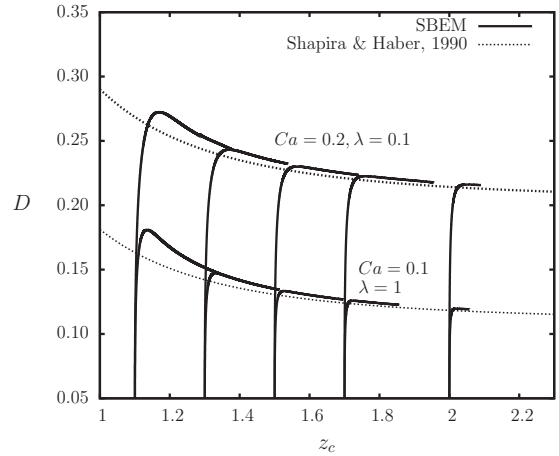

FIG. 14. Deformation D as a function of droplet centroid location z_c for z_{c0}=1.1, 1.3, 1.5, 1.7, and 2. Two cases are presented: (i) Ca=0.2 and λ=0.1 and (ii) Ca=0.1 and λ=1. Also included are analytical predictions of $O(z_c^{-3})$ by Shapira and Haber (Ref. 2) for comparison.

tance. Figure 12(b) shows that the lengths of both axes experience rapid change upon release (i.e., the long axis elongates while the short axis shrinks) followed by a slower retraction. The long axis deformation is shown to contribute more in the deformation overshoot. As shown in Fig. 13 a pointing tip is formed near the wall on the droplet interface, which is responsible for the overshooting peaks in the long axis and the deformation. It is also evident that droplets with better deformability tend to have greater overshoot near the solid wall. The overshoot and relaxation of the droplet deformation are also observed in numerical computations for droplets confined in two parallel plates (e.g., Janssen and Anderson,[11] Griggs *et al.*).[21] For orientation angles, as shown in Fig. 12(c) we observe that for all initial distances z_{c0}, θ_S first increases rapidly and then gradually decreases. For the long axis orientation angle θ_L, we found that for a larger distance to the wall θ_L undergoes a fast decrease initially followed by a slow decrease. However, starting at a small distance to the wall, θ_L increases initially and some noise in the data value have been shown followed by a slow decrease. The noise in orientation angle calculations resulted from the nature of numerical computation, which is also observed by Janssen and Anderson[11] in their computations. The behavior of droplet deformation and orientation angles show that instantly upon the release, the droplet rapidly deforms and rotates. After the maximum deformation is achieved the droplet tends to rotate backward while the deformation slowly reduces. The magnitudes of the variations in the deformation and orientation angles are more prominent when the initial location of the droplet is closer to the wall.

The droplet deformation D as a function of its lateral position z_c is plotted in Fig. 14 for two cases (i) capillary number Ca=0.2 and viscosity ratio λ=0.2 and (ii) Ca=0.1 and λ=1. A variety of initial locations has been examined. We observe that the initially spherical droplet shows a substantial deformation without much lateral migration away from the wall. As the droplet migrates away from the wall relaxation in deformation takes place. We found in the relaxation process, the relation between the droplet deformation D and the lateral position z_c is independent on the initial location of the droplet. In Fig. 14 we include the analytical predictions of the droplet deformation based on the formula derived by Shapira and Haber[2] which accounts for the modification to the droplet deformation in shear flow due to the existence of a single solid wall nearby. The analytical results agree well with the numerical calculations when the droplet deformation retracts to small values, i.e., when the droplet migrates further away from the wall or the capillary number is small. The discrepancy at large deformation lies in the fact that the analytical study of Shapira and Haber[2] is primarily based on the small deformation theory of Taylor,[24] as well as the fact that their analytical formula is only valid for large distances between the droplet and the wall.[1]

The relative difference between the deformation of a droplet near the solid wall and that of a droplet freely suspended in shear flow, $(D-D^{\infty})/D^{\infty}$, is plotted as a function of the droplet-wall distance z_c in Fig. 15. We consider only the relaxation process of the droplet since as found in Fig. 14 the relaxation deformation is independent on the initial location. It is found that the existence of a solid wall amplifies the droplet deformation significantly. Among the cases plotted in Fig. 15, about 46% increase in the droplet deformation is observed for λ=1 if the droplet is located z_c=1.25 from the wall. The droplet deformation decreases as z_c increases and eventually becomes identical with the deformation of a droplet freely suspended at around z_c=5 for all cases. We also

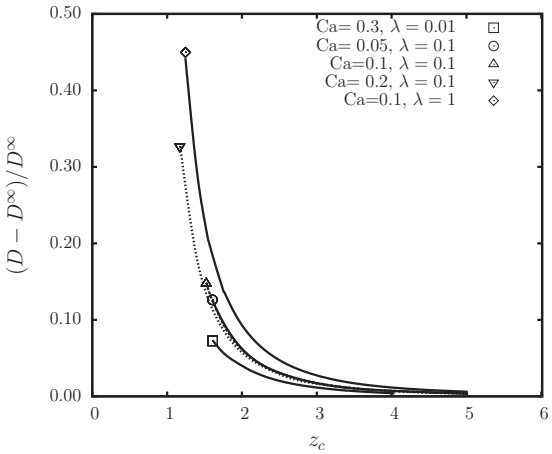

FIG. 15. Relative difference in deformation, $(D-D^\infty)/D^\infty$, as a function of the droplet-wall distance z_c. D^∞ is the steady-state deformation of a droplet freely suspended in an unbounded shear flow. Curves are included for a variety of capillary numbers and viscosity ratios.

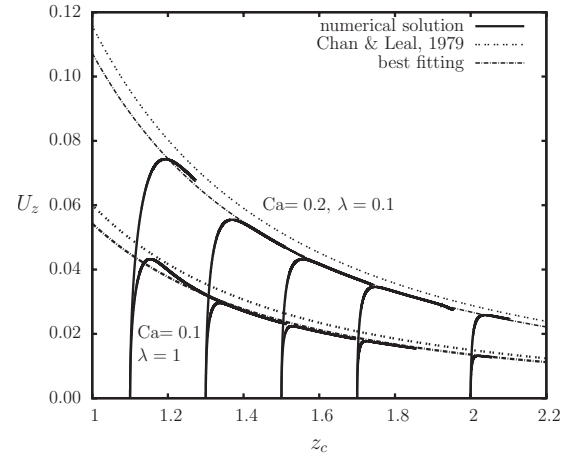

FIG. 17. Migration velocity U_z as a function of droplet centroid location z_c for z_{c0}=1.1, 1.3, 1.5, 1.7, and 2. Two cases are presented: (i) Ca=0.2 and λ=0.1 and (ii) Ca=0.1 and λ=1. A best z_c^{-2} fitting for the decreasing part of U_z is shown. Analytical predictions by Chan and Leal (Ref. 25) are also included.

found that the relative difference in the deformation is independent on the capillary number Ca. As shown in Fig. 15, for λ=0.1, curves for a variety of Ca overlap. The independence on Ca is also found for other viscosity ratios (which are not included in the Figure). Figure 15 also shows that the amplification effect of the existence of a wall is more prominent for larger λ if λ≤1 for all z_c values. More discussion on the influence of λ can be found in Sec. IV D.

Although the deformation during relaxation is independent on the initial droplet location, the time an initially spherical droplet spent before the relaxation stage is reached can be related to the initial location. As shown in Fig. 16 where the transient deviation of the deformation from that of a fully relaxed droplet $|D-D_{zc}|$ is plotted for a variety of initial locations, a droplet with a smaller initial distance toward the wall tends to reach the relaxation stage earlier.

The wall effect is also more substantial for the lateral migration velocity U_z, which instantly increases to its maximum upon release. The maximum U_z is larger if the initial droplet location is closer to the wall. After the maximum U_z is reached, the lateral velocity starts to decrease. Figure 17 plots U_z as a function of z_c at a variety of droplet initial locations for a droplet with Ca=0.1 and λ=1 and that with Ca=0.2 and λ=0.1. We observe that, independent on the initial location, U_z always increases abruptly, which makes the droplet to drift away from the solid wall rapidly. And the slower decrease in U_z is also independent on the initial location of the droplet. The decreasing behavior of U_z is proportional to z_c^{-2} as predicted by Chan and Leal.[25] Curves utilizing the z_c^{-2} dependence formula of the velocity U_z by Chan and Leal[25] has been plotted in Fig. 17. A small discrepancy has been observed and the analytical solution by Chan and Leal[25] shows an overestimation comparing to our numerical solution. We also show the best z_c^{-2} fitting on the same figure for the decreasing lateral velocity U_z and find that the best fitting can always be expressed as

$$U_{z,\text{decreasing}} = kU_{z,CL}, \tag{11}$$

where k is a coefficient which is dependent on the capillary number and the viscosity ratio. $U_{z,CL}$ denotes the analytical prediction by Chan and Leal. For the two cases presented, k=0.926 76 and 0.903 67 for the upper and lower curves, respectively.

In Fig. 18, the longitudinal velocity U_x is plotted as a function of droplet centroid location z_c for four different initial locations of a droplet with Ca=0.1 and 0.2, and λ=1. We observe that the increasing part of the velocity U_x is almost independent on the initial location of the droplet and they can be described by the single curve as a function of the droplet centroid location z_c. It can also be observed that the curves for increasing U_x with different Ca tend to converge as z_c increases. The dependency on Ca for U_x is only prominent when the droplet is very close to the wall. The analytical prediction for the increasing U_x by Shapira and Haber[2] is also included. Good agreement has been found between our numerical solution and the analytical prediction. The analytical solution slightly underestimates the increasing U_x for larger capillary numbers in close vicinity of the wall.

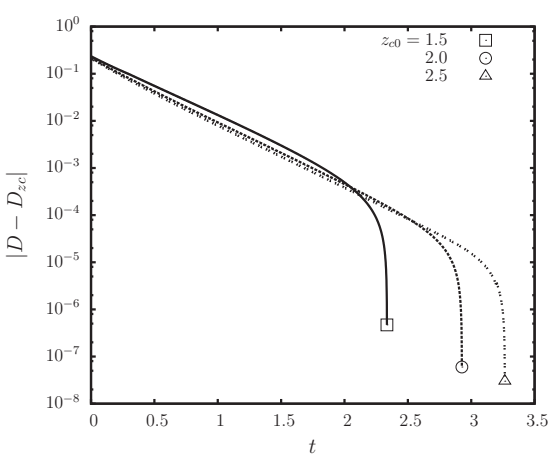

FIG. 16. Deviation of the droplet deformation from relaxation deformation $|D-D_{zc}|$ as a function of time. Various initial droplet-wall distances are included z_{c0}=1.5, 2.0, and 2.5 for Ca=0.2 and λ=0.1.

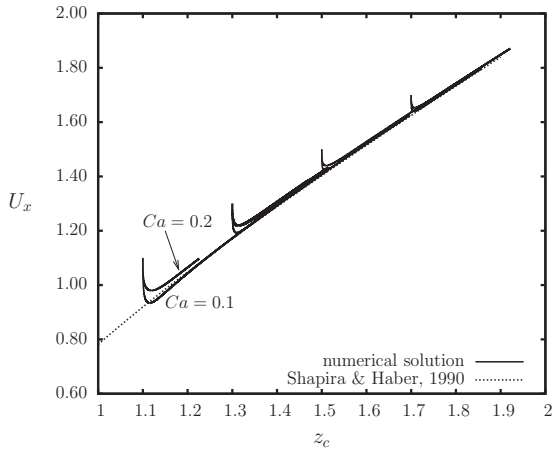

FIG. 18. Longitudinal velocity U_x as a function of droplet centroid location z_c. Ca=0.1 and 0.2, $\lambda=1$, and z_{c0}=1.1, 1.3, 1.5, and 1.7. Also included as the dotted line is the analytical prediction by Shapira and Haber (Ref. 2) for the increasing U_x.

D. Influence of the viscosity ratio

We plot the droplet deformation D as a function of time t for a variety of viscosity ratios $\lambda=0.1$, 0.5, 1, 1.5, 5, and 10 in Figs. 19(a) and 19(b). It can be observed that as the viscosity ratio increases, the rate of deformation decreases monotonically. However the magnitude of the deformation

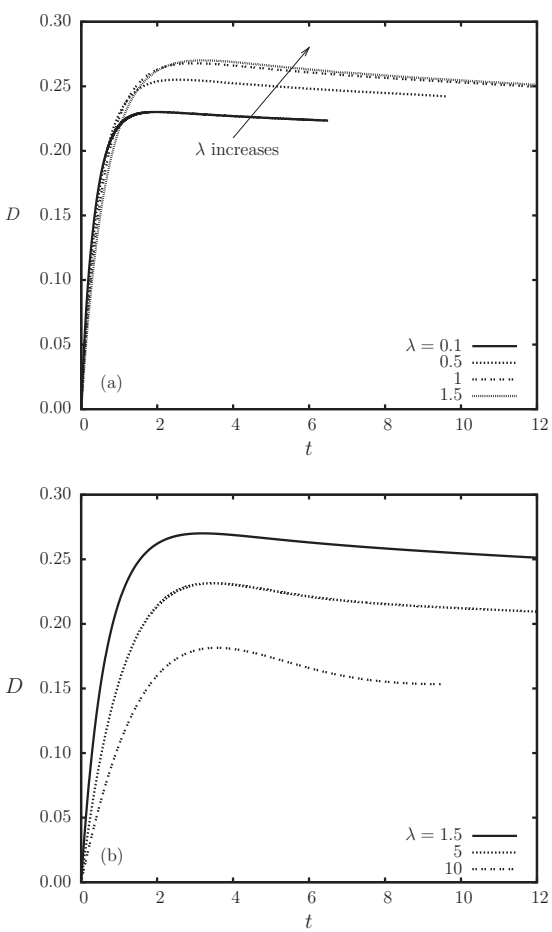

FIG. 19. Deformation D as a function of time t. Ca=0.2, $\lambda=0.1$, 0.5, 1, 1.5, 5, and 10, and z_{c0}=1.5.

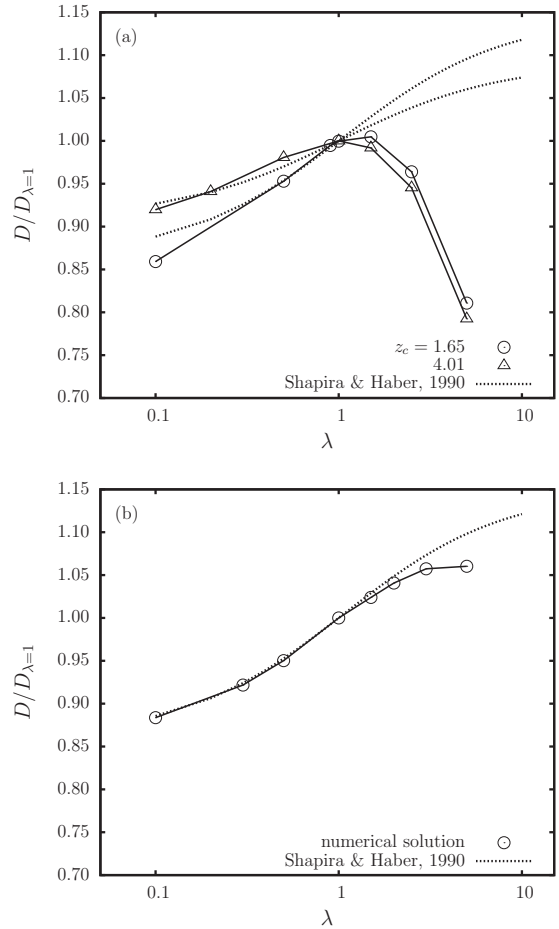

FIG. 20. Deformation D normalized by the deformation at $\lambda=1$ as a function of viscosity ratio λ for (a) Ca=0.2 and z_{c0}=1.65 and 4.01, and (b) Ca=0.05 and z_{c0}=1.61. The numerical results are plotted as circles and triangles connected with solid lines. Analytical solutions using the derivation by Shapira and Haber (Ref. 2) are included as dotted curves.

does not vary with the viscosity ratio monotonically. The maximum deformation increases with λ when $\lambda<1.5$ as shown in Fig. 19(a), but decreases as λ increases when $\lambda\geq 1.5$ as shown in Fig. 19(b). The nonmonotonical behavior of the deformation D as a function of viscosity ratio is contrary to the analytical prediction by Shapira and Haber.[2] This is shown in Fig. 20(a), where we plot the droplet deformation D as a function of the viscosity ratio λ for a droplet migrates to the location z_c=1.65 and 4.01. The capillary number is Ca=0.2. To discount the discrepancy in terms of capillary number, we plot the droplet deformation normalized by its deformation at $\lambda=1$. The analytical study by Shapira and Haber[2] predicts that the deformation increases monotonically with λ while we observe a maximum deformation is achieved around $\lambda=1$ in the numerical solution. The analytical prediction and numerical results agree with each other for $\lambda<O(1)$. In addition, the numerical solution shows that for $\lambda\leq 1.5$ the deformation is smaller for a droplet closer to the wall while for $\lambda>1.5$ the deformation is larger for a droplet closer to the wall. This finding is in qualitative agreement with the analytical prediction shown as dotted lines in Fig. 20. Comparisons have also been made with the analytical solution for a small capillary number

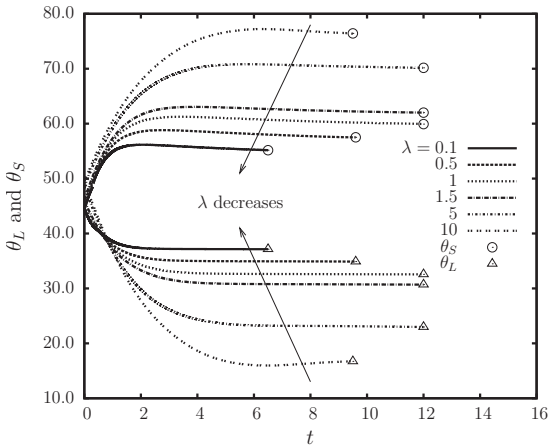

FIG. 21. Orientation angles (θ_L and θ_S) as a function of time t. Ca=0.2, λ=0.1, 0.5, 1, 1.5, 5, and 10, and z_{c0}=1.5.

Ca=0.05 as shown in Fig. 20(b). It shows that for small to intermediate viscosity ratios the numerical solution agrees well with the analytical solution. However, the analytical work still overpredicts the deformation at large λ. We believe that besides the small deformation theory that the analytical method adopts, the discrepancy is also incurred by their assumption of a constant orientation angle θ_L=45°. Numerical results show in Fig. 21 that the deviation from 45° for both θ_L and θ_S is more significant for larger λ. Our findings are in qualitative agreement with the numerical study by Griggs *et al.*[21] who showed the nonmonotonic deformation of a droplet in a Poiseuille flow between parallel plates regarding the viscosity ratio over $0.5<\lambda<10$.

The viscosity ratio is also found to influence the time that a droplet spends before the relaxation stage is reached. As shown in Fig. 22, the difference between the droplet deformation D and that for a fully relaxed droplet D_{zc} is plotted as a function of time. For $\lambda \leq 1$, the time needed to reach the relaxation stage increases as we increase the viscosity ratio

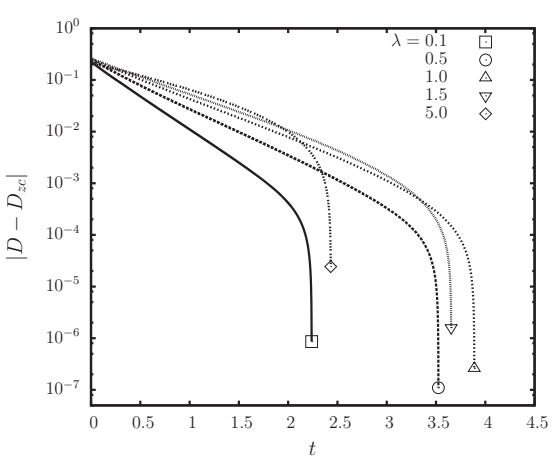

FIG. 22. Deviation of the droplet deformation from the relaxation deformation $|D-D_{zc}|$ as a function of time. A variety of viscosity ratios is included for comparison: λ=0.1, 0.5, 1.0, 1.5, and 5.0. For all cases, Ca=0.2 and z_{c0}=1.7.

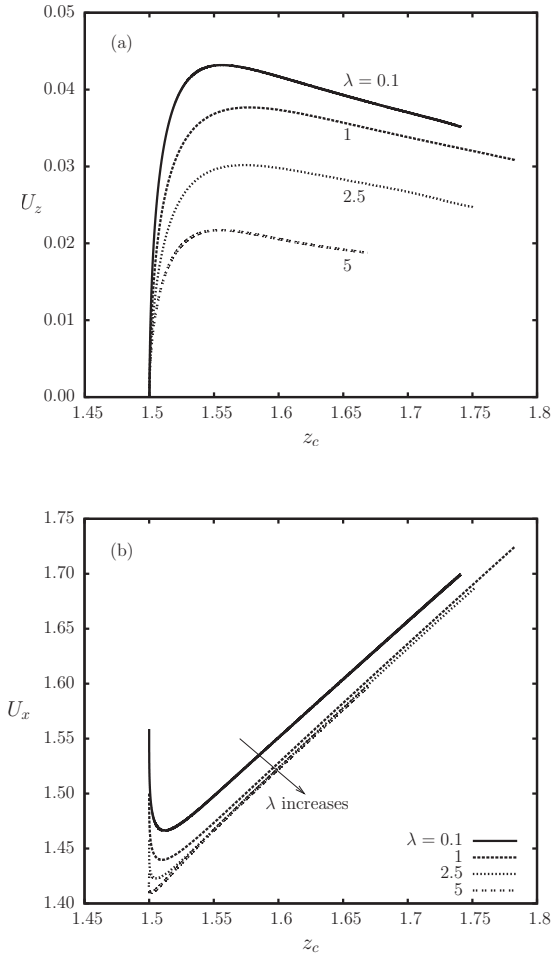

FIG. 23. The lateral and longitudinal velocities (U_z and U_x) as functions of droplet centroid location z_c and the viscosity ratio λ. For all cases, the capillary number is Ca=0.2.

λ, while for $\lambda \geq 1$, a decrease in the time is observed as λ increases. The maximum time needed to reach relaxation is found around $\lambda=1$.

On the contrary, the lateral velocity U_z and longitudinal velocity U_x of the droplet decrease monotonically with the increase of the viscosity ratio as shown in Fig. 23 where we plot the velocities as functions of droplet centroid z_c for λ=0.1, 1, 2.5, and 5, and Ca=0.2. The monotonic behavior of U_z differs from the analytical solution by Chan and Leal,[25] which predicts that the lateral migration velocity U_z increases with the viscosity ratio, as shown in Fig. 24. The discrepancy is also found by Uijttewaal and Nijhof[20] by comparing their numerical solution to the analytical prediction. The prediction by Shapira and Haber on U_x as a function of λ qualitatively agrees with our numerical solution as shown in Fig. 25, where we plot the longitudinal velocity U_x normalized by U_x at $\lambda=1$ to discount the influence of the capillary number. We observe that for $\lambda<O(1)$ the analytical results overestimates the longitudinal velocity U_x while underestimation is found for the analytical prediction for $\lambda>O(1)$.

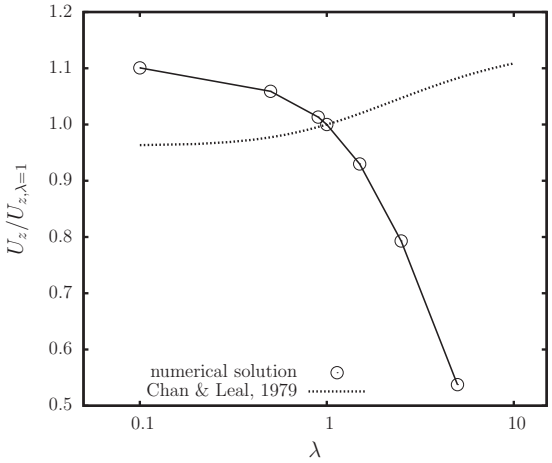

FIG. 24. Velocity U_z as a function of viscosity ratio λ for Ca=0.2 and $z_{c0}=1.65$. Numerical results are plotted as circles connected with solid lines. The analytical prediction by Chan and Leal (Ref. 25) is also included as the dotted curve.

V. CONCLUSIONS

The motion of an initially spherical droplet in a shear flow confined by a single solid wall is investigated using a 3D spectral boundary element method which benefits from the characteristics of spectral methods (i.e., exponential convergence and numerical stability as the number of discretization points increases). Comparisons have been made for the droplet motion near a single wall and that between two parallel plates. It is found that a faraway plate could be neglected if it is located at a distance larger than 15 times of the droplet characteristic length to the droplet. We also validate our numerical method by comparing the results to both numerical and experimental studies. The validation shows that our method is able to describe well the droplet deformation, migration, and translation in microconfined shear flow.

Investigations are conducted for the influences of the capillary number, viscosity ratio and initial location of the droplet on the droplet deformation, orientation, lateral velocity, and longitudinal velocity. The droplet behavior can be divided into two stages after it is released near a solid wall: (i) the initial rapid deformation and (ii) the relaxation process. In the first stage, the droplet deforms and rotates rapidly with velocities built up abruptly. And then in the relaxation stage, the change in droplet geometry and velocity slows down. Our analysis indicates that the relaxation stage appears later for larger Ca values and larger z_{c0} values. However, the influence of λ on the time needed for a droplet to reach the relaxation stage is more complicated. The maximum time needed is achieved at $\lambda=1$. Similar to the droplet deformation in unbounded shear flow, the increase in the capillary number leads to the increase in the droplet deformation D. The existence of a single wall in a close vicinity of the droplet creates an overshoot in the increase of the droplet deformation upon the release of the droplet. The overshoot is more prominent for larger capillary number and smaller distance between the droplet and the wall. The droplet long axis always tends to rotate toward the flow direction, while the short axis rotates rapidly away the flow direction upon release but it tends to slowly rotate back in the relaxation process. The droplet behavior in the relaxation process is found to be a function of droplet centroid in the lateral direction, capillary number, and viscosity ratio. The initial location of the droplet does not influence the droplet relaxation. Numerical results have been compared to analytical predictions. Agreement has been found that as the droplet moves away from the wall both the deformation D and lateral velocity U_z decreases and the longitudinal velocity U_x increases. Small discrepancy has been found between the numerical and analytical results due to the assumptions of small deformation and large droplet-wall distance that analytical predictions employed. For large Ca values the droplet deformation is found to reach a maximum around $\lambda=O(1)$ as we increase the viscosity ratio. Both the lateral velocity and the longitudinal velocity decrease with the viscosity ratio monotonically. Disagreement has been found between the numerical results and analytical predictions for the influence of the viscosity ratio on the droplet deformation for $\lambda>O(1)$, as well as on the droplet lateral velocity for the entire range of viscosity ratio examined.

We conclude that the 3D spectral boundary element formulation has been successfully applied to investigate the droplet motion in microconfined shear flow. Numerical studies are necessary for this type of problem if high accuracy is desired. The comparison between the numerical and analytical solutions suggests that the analytical predictions are limited for small deformations, large droplet-wall distances, and near equiviscous droplets. More experimental work is suggested to be conducted in the future for the motion of nonequiviscous droplets in a close vicinity of a solid wall, especially for a droplet more viscous than the suspending fluid.

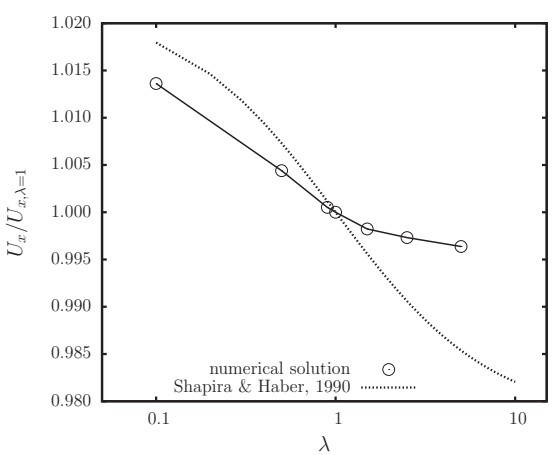

FIG. 25. Velocity U_z as a function of viscosity ratio λ for Ca=0.2 and $z_{c0}=1.65$. Numerical results are plotted as circles connected with solid lines. The analytical prediction by Shapira and Haber (Ref. 2) is also included as the dotted curve.

ACKNOWLEDGMENTS

This work was supported by ND EPSCoR and NSF EPS Grant No. 0814442 and NDSU Development Foundation's Centennial Endowment. Some computations were performed on multiprocessor computers at Teragrid.

[1]M. Shapira and S. Haber, "Low Reynolds number motion of a droplet between two parallel plates," Int. J. Multiphase Flow **14**, 483 (1988).
[2]M. Shapira and S. Haber, "Low Reynolds number motion of a droplet in shear flow including wall effects," Int. J. Multiphase Flow **16**, 305 (1990).
[3]F. Su and K. Chakrabarty, "Microfluidics-based biochips: Technology issues, implementation platforms, and design-automation challenges," IEEE Trans. Comput.-Aided Des. **25**, 211 (2006).
[4]H. Song, J. D. Tice, and R. F. Ismagilov, "A microfluidic system for controlling reaction networks in time," Angew. Chem., Int. Ed. **42**, 768 (2003).
[5]T. M. Squires and S. R. Quake, "Microfluidics: Fluid physics at the nanoliter scale," Rev. Mod. Phys. **77**, 977 (2005).
[6]H. A. Stone, A. D. Stroock, and A. Ajdari, "Engineering flows in small devices: Microfluidics toward a lab-on-a-chip," Annu. Rev. Fluid Mech. **36**, 381 (2004).
[7]Y. Tan, J. S. Fisher, A. I. Lee, V. Cristini, and A. P. Lee, "Design of microfluidic channel geometries for the control of droplet volume, chemical concentration, and sorting," Lab Chip **4**, 292 (2004).
[8]D. R. Link, S. L. Anna, D. A. Weitz, and H. A. Stone, "Geometrically mediated breakup of drops in microfluidic devices," Phys. Rev. Lett. **92**, 054503 (2004).
[9]S. Y. Teh, L. H. Hung, R. Lin, and A. P. Lee, "Droplet microfluidics," Lab Chip **8**, 198 (2008).
[10]T. D. Chung and H. C. Kim, "Recent advances in miniaturized microfluidic flow cytometry for clinical use," Electrophoresis **28**, 4511 (2007).
[11]P. J. A. Janssen and P. D. Anderson, "Boundary-integral method for drop deformation between parallel plates," Phys. Fluids **19**, 043602 (2007).
[12]V. Sibillo, G. Pasquariello, M. Simeone, V. Cristini, and S. Guido, "Drop deformation in microconfined shear flow," Phys. Rev. Lett. **97**, 054502 (2006).
[13]A. Vananroye, P. J. A. Janssen, P. D. Anderson, P. V. Puyvelde, and P. Moldenaers, "Microconfined equiviscous droplet deformation: Comparison of experimental and numerical results," Phys. Fluids **20**, 013101 (2008).
[14]P. J. A. Janssen and P. D. Anderson, "A boundary-integral model for drop deformation between two parallel plates with non-unit viscosity ratio drops," J. Comput. Phys. **227**, 8807 (2008).
[15]D. Megias-Alguacil, K. Feigl, M. Dressler, P. Fischer, and E. J. Windhab, "Droplet deformation under simple shear investigated by experiment, numerical simulation and modeling," J. Non-Newtonian Fluid Mech. **126**, 153 (2005).
[16]A. Vananroye, P. V. Puyvelde, and P. Moldenaers, "Effect of confinement on droplet breakup in sheared emulsions," Langmuir **22**, 3972 (2006).
[17]D. Leighton and A. Acrivos, "The lift on a small sphere touching a plane in the presence of a simple shear flow," Z. Angew. Math. Phys. **36**, 174 (1985).
[18]J. R. Smart and D. T. Leighton, Jr., "Measurement of the drift of a droplet due to the presence of a plane," Phys. Fluids A **3**, 21 (1991).
[19]W. S. J. Uijttewaal, E. J. Hijhof, and R. M. Heethaar, "Droplet migration, deformation, and orientation in the presence of a plane wall: A numerical study compared with analytical theories," Phys. Fluids A **5**, 819 (1993).
[20]W. S. J. Uijttewaal and E. J. Hijhof, "The motion of a droplet subjected to linear shear flow including the presence of a plane wall," J. Fluid Mech. **302**, 45 (1995).
[21]A. J. Griggs, A. Z. Zinchenko, and R. H. Davis, "Low-Reynolds-number motion of a deformable drop between two parallel plane walls," Int. J. Multiphase Flow **33**, 182 (2007).
[22]C. Pozrikidis, *Boundary Integral and Singularity Methods for Linearized Viscous Flow* (Combridge University Press, New York, 1992).
[23]Y. Wang and P. Dimitrakopoulos, "A three-dimentional spectral boundary element algorithm for interfacial dynamics in stokes flow," Phys. Fluids **18**, 082106 (2006).
[24]G. I. Taylor, "The formation of emulsions in definable fields of flows," Proc. R. Soc. London, Ser. A **146**, 501 (1934).
[25]P. C.-H. Chan and L. G. Leal, "The motion of a deformable drop in a second-order fluid," J. Fluid Mech. **92**, 131 (1979).